

Performance of the GSC engineering-counter for MAXI/ISS

Tatehiro Mihara^a, Nobuyuki Kawai^a, Atsumasa Yoshida^a, Ikuya Sakurai^a, Toshikazu Kamae^a,
Masaru Matsuoka^b, Yuji Shirasaki^b, Mutsumi Sugizaki^b, Weiming Yuan^b, Isao Tanaka^c

^aRIKEN, Wako, Saitama, 351-0198, Japan

^bNASDA, Tsukuba, Ibaraki, 305-8505, Japan

^cGraduate University for Advanced Studies, Tsukuba, Ibaraki, 305-0801, Japan

ABSTRACT

We are developing Monitor of All Sky X-ray Image (MAXI) which will be mounted on the Japanese Experiment Module of the International Space Station. MAXI is an all-sky X-ray monitor which scans the sky in every 90 minutes. The sensitivity will be as high as 7 mCrab (5 σ level) in one scan and 1 mCrab in one-week accumulation. The GSC (Gas Slit Camera) instrument consists of twelve one-dimensional position sensitive proportional counters using the Xe+CO₂ gas and the carbon fiber anodes of 10 μ m diameter. The window size is 272 \times 190 mm. The position is obtained by the charge division method. It is used to identify the source in the long rectangular field-of-view (1.5 \times 80 degrees). Three cameras will be set to cover the 1.5 \times 160 degrees arc. The position resolution is essentially important, which becomes better in the higher gas gain. We have tested gas mixtures of Xe+CO₂ with CO₂ = 0.2%, 0.5%, 1%, and 3%. The CO₂ = 0.5% showed the most uniform gas gain, but has a little after pulses. We chose the Xe (99%) + CO₂ (1%) combination for the flight counters. It can achieve the uniform gas gain in the cell and negligible after-pulse in high operating voltage. The engineering model of the counter (EM1) was build. We have tested the position resolution and the energy resolution across the counter. The position resolution and the energy resolution depend on the X-ray energy. On the basis of these results, together with the collimator response, we performed a realistic simulation.

Keywords: MAXI, International Space Station, X-ray, All-sky monitor, proportional counter, anomalous gas gain

1. MONITOR OF ALL-SKY X-RAY IMAGE (MAXI)

Monitor of All-sky X-ray Image (MAXI) is the first astronomical payload to be placed on the International Space Station (ISS)'s Japanese Experimental Module (JEM) in 2005 (Fig. 1 left) [1, 2, 3, 4]. MAXI has the size of 0.8 \times 1.2 \times 1.85 m and the weight of 500kg. Power, communication, and cooling fluid are supplied from the JEM/ISS. MAXI has two X-ray observational instruments, Gas Slit Camera (GSC) and Solid-state Slit Camera (SSC, Miyata in this meeting). The GSC uses gas counters which is sensitive in 2–30 keV. The SSC uses X-ray CCDs sensitive in the soft X-ray (0.5–10 keV). Both instruments are slit-cameras and have a long rectangular field-of-view (FOV) (Fig. 1 middle). With the combination of one-dimensional X-ray detector, the positions of the X-ray sources in the FOV are determined (Fig. 1 right). The narrow FOV scans across the sky with the 90-minute orbital rotation of the ISS. The GSC has two identical FOVs, one is facing forward and the other zenithal. The forward FOV is tilted up by 6 degrees to avoid the earth and the atmosphere completely. There are non-operational periods in the orbit, such as the South Atlantic Anomaly and the high-radiation polar regions. Although one FOV cannot observe the portion of the sky which to be observed from there, the other FOV can cover that region after or before 21 minutes, because it is offset by 84 degrees. Thus MAXI can monitor almost the whole sky in every 90 minutes, twice in most part.

As an all-sky monitor MAXI has unprecedented sensitivity in the hard X-ray band (0.5–30 keV). The purposes of the all-sky monitor are not only the discoveries of new X-ray sources, but also the challenge to the cosmology models by measuring the large scale structure of the universe via the distribution of distant active galaxies as well as the cosmic X-ray background. The sensitivity is 7 mCrab (5 σ level) in one scan and 1 mCrab in one-week accumulation [1, 3]. The former is as sensitive as can detect the X-ray afterglow of the gamma-ray burst if it scans within 290 s after the burst. The latter is as sensitive as can detect hundreds of faint extra-galactic objects (AGNs and galaxy clusters). The AGNs (quasars, BL Lac objects, Seyfert galaxies) are variable in a time scale of 100 s \sim years. It is the first experiment to monitor the variability of the extra-galactic sources without a bias.

Further author information: T.M.: E-mail: mihara@crab.riken.go.jp

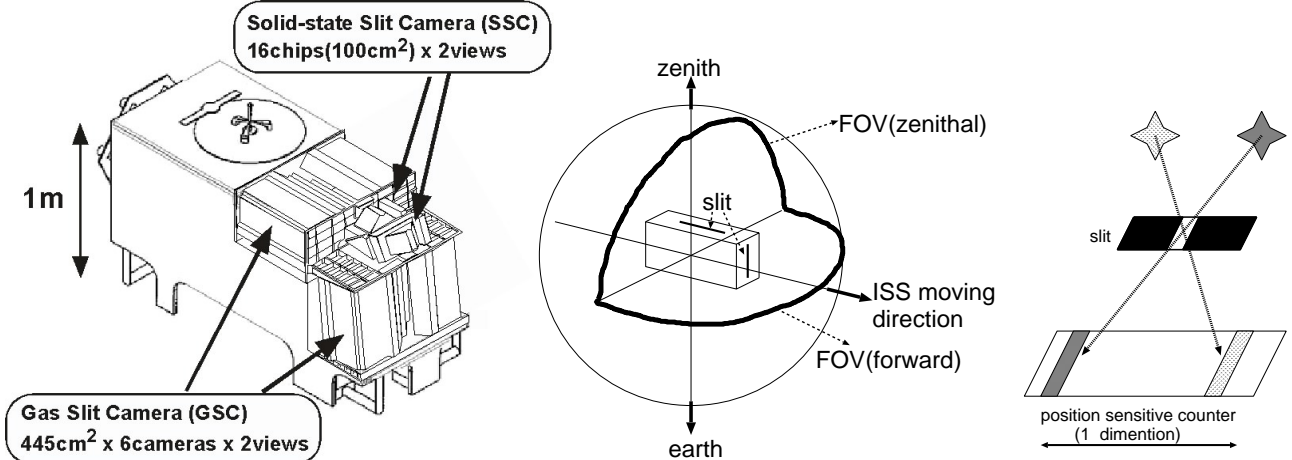


Figure 1. left: The MAXI payload has two scientific instruments, GSC and SSC. middle: Both instruments have two field of views (FOV) which cover the one's dead area due to the South Atlantic Anomaly by the other. right: One-dimensional X-ray detector is used to determine the source positions in the rectangular FOV.

2. GAS SLIT CAMERA (GSC)

GSC consists of twelve cameras with proportional counters. Two cameras are set in a 'pillar' (a unit) as arrows in Fig. 1 left indicate, and watch the same FOV. The triangular part above the counters contains slats collimators to limit the FOV to 1.5 × 80 degrees. There is a slit on the top of the triangle to transmit the X-ray from the sources onto the counter. Three units (i.e. six cameras) are placed to cover 1.5 × 160 degrees. The 10 degrees from the edge are abandoned, because some of them are shadowed by other modules on ISS.

Fig. 2 is the top view of one GSC flight model counter. The window size is 272 × 190 mm, which is about A4-paper size. The opening area is 445.9 cm². Twelve counters make 5350 cm² in total. The gas is the mixture of Xe and CO₂ with total pressure of 1.4 atm at 0 °C. The carbon fibers with 10 μm in diameter are used for anodes. The resistances are about 33 kΩ, and the length is 333 mm. The position is obtained by the charge division method. The preamplifiers (A225 hybrid IC) are connected to both ends of the anode. The pulse height from the left L and that from the right R are obtained. The position measure PM is defined as $PM = (R - L)/(R + L)$. The incident X-ray position is determined by PM using the calibrated curve.

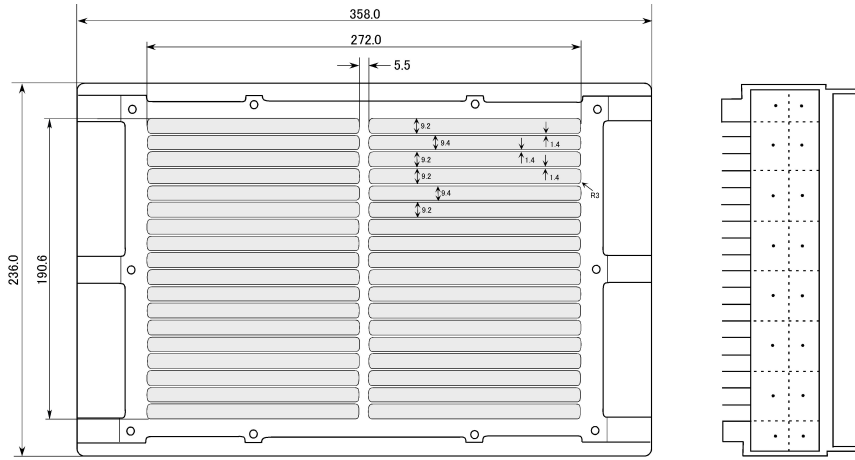


Figure 2. Top view of the MAXI/GSC Flight Model counter. The unit is [mm]. Gray parts are Be window, which is supported by the beams of 1.4mm width and 17mm height. The Be window area is 445.9 cm². There are 6 cells with carbon anodes, which are surrounded by the 10 veto cells. Each cell has three beams. The counter is made of titanium. It was chosen because it has a similar expansion coefficient with beryllium.

3. ANOMALOUS GAS GAIN

To obtain the good position resolution with this proportional counter, high pulse height is needed. The noise is dominated by the Johnson noise of the resistive anode. Therefore the position resolution has $\Delta X/X \propto PH^{-1}R^{0.5}$ relation. Thinner wires with higher resistance can improve the position resolution, but $10 \mu\text{m}$ is almost the limit of the handling. As will be shown in §4, the GSC will be operated in rather high gas gain (~ 6000), compared with that of the usual proportional counters (gas gain of ~ 1000). When we raised the high voltage, we encountered the hard tail problem.

3.1. Hard tail with $\text{CO}_2 = 3\%$ gas

A hard tail as shown in Fig. 3 emerged at high voltage (1600V) with the common $\text{Xe} + \text{CO}_2 = 3\%$ gas. The pulse height ratio of the hard tail to the normal peak became larger at higher voltage. It exists when we irradiate X-ray near the anode wire, and not exist off the wire (Fig. 3). The proportional counter of the same gas but with metal anode also showed the hard tail in the high gas gain. Thus, it is not the problem of the anode wire, but the gas.

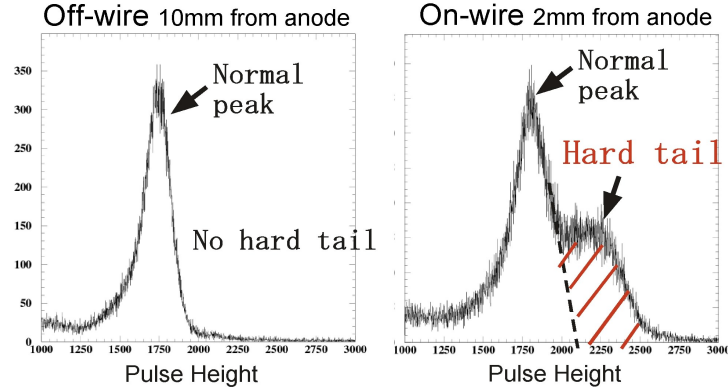


Figure 3. Hard tail appeared when operating in rather high gas gain (HV = 1600V). It exists only when the X-ray is irradiated near the anode (left: off-wire, right: on-wire). The gas was $\text{CO}_2 = 3\%$, and the X-ray was Mo-K.

3.2. Slant beam method

To investigate this phenomena, we used the slant beam method. We tilted the X-ray beam within the plane which the anode and the beam make. Fig. 4 shows the case when the beam crosses the anode wire. We used $\theta = 45$ degrees. Let X the direction of the anode and Z the depth from the window. By using the one-dimensional position sensitive counter, we know X for each X-ray event. Since X and Z correspond to each other in the slant beam method, we know the depth Z , where the X-ray is absorbed.

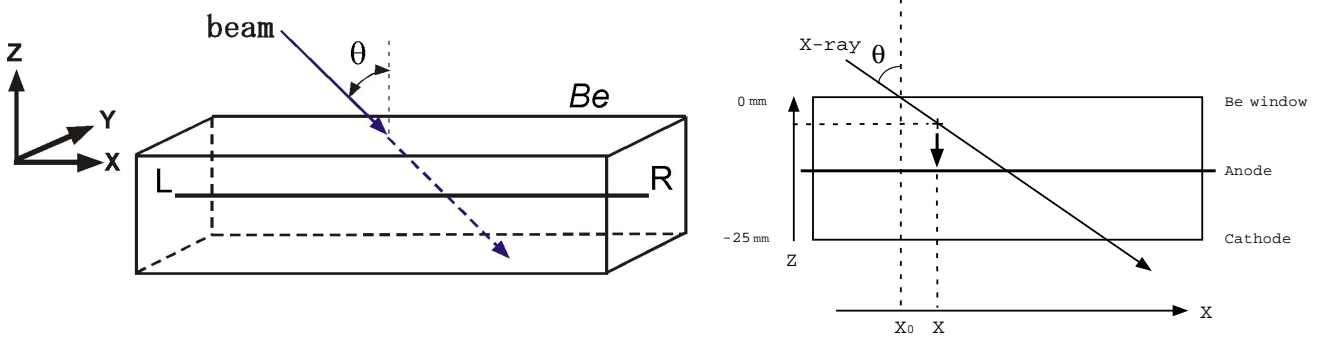


Figure 4. Slant beam method: When the beam is tilted, the detected position X correspond to the stopped depth Z . One-dimensional position sensitive counter can tell the position X of each X-ray, and we can know the depth Z .

3.3. M-curves

Fig. 5 upper is the event plots by the slant beam method in Z and PH plane. The PH changed with the depth Z . The gas gain is normal at the window and the bottom of the cell, rises towards the anode, has maximum at 3mm from the anode, and then goes down. The hard tail was due to the different gas gain on the position where the X-ray was absorbed. The Y-scan of the slant beam method can make a gain map in the cell. It showed that the gain variation is symmetric on the anode and very similar to the shape of the electric field [5]. We define the anomalous gas gain factor g , as $PH = Q_0 (1 + g)$, where Q_0 is the pulse height of the normal peak. The g is the function of Z , and the maximum of g is denoted as g_{max} . What causes the anomalous gas gain? Fig. 5 also shows the HV dependency. The anomalous gas gain factor increased with high voltage. Actually it was proportional to the normal gas gain Q_0 itself [5]. This means that the additional pulse height of the hard tail from the normal peak increases as $\propto Q_0^2$. We used Mo-K X-ray because Ti-K and Cu-K cannot penetrate very far. The X-ray mean free path in Xe of 1.4 atm is 4.7 mm for Ti-K, 8.0 mm for Cu-K α , and 28.8 mm for Mo-K α .

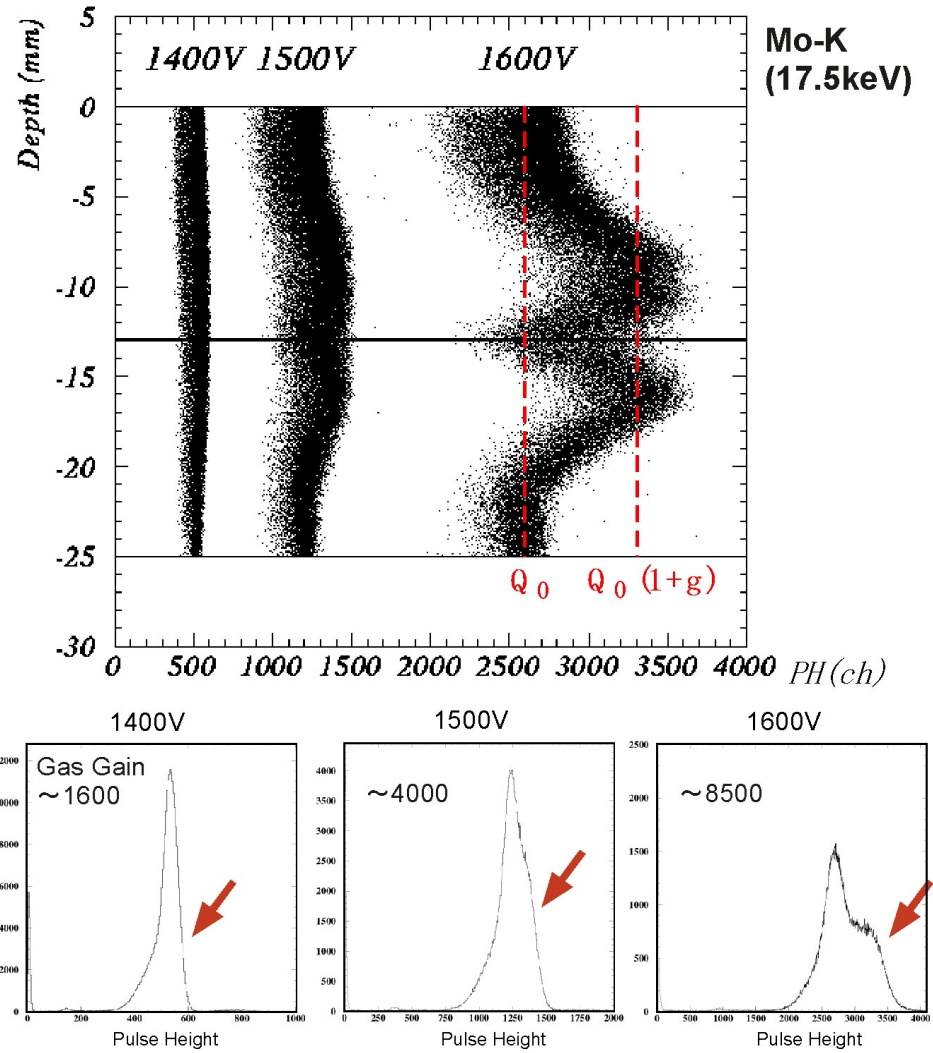


Figure 5. The upper is the M-curves with 1400V, 1500V, 1600V of the $Xe + CO_2 = 3\%$ gas. The gas gains of the normal peak are about 1600, 4000, 8500. The bottom is the spectra obtained by integrating the M-curves over the depth. The X-ray is Mo-K α . The ‘soft tail’ in the spectrum is the continuum which is left over after the Zr filter. We define the anomalous gas gain factor g as shown in the figure. Q_0 is the pulse height of the normal peak. The pulse height at depth Z is written as $Q_0 (1 + g)$, where g is the function of Z .

3.4. Ar + CO₂ and Ar + CH₄ combinations

We investigated this phenomenon with Ar + CO₂ and Ar + CH₄ gases in the gas-flow counter. Fig. 6 upper shows the M-curves with CO₂ = 3%, 5%, 10%, and 20%. M-curve is also seen, but higher density of CO₂ is needed to have the similar M-shape (10% in Ar instead of 3% in Xe). Moreover, the CO₂ = 3% showed V-curve. The V-curve can be understood as the expanded M-curve. The position of g_{max} is expanded outward in the smaller density of CO₂.

We also tried Ar + CH₄ = 5%, 10%, 20% combinations. All of them showed V-curve (Fig. 6 lower), although the depth of V-curve is shallow in the high CH₄ density. Higher density of CH₄ (30%) and higher total pressure (7atm) can make the curve M-shaped [7].

Thus the M-curve is the common phenomenon in the cylindrical proportional counters operating in the high gas gain. However, the extent of M-shape and the amount of g_{max} in the same gas gain are different with the combination of the main gas (Xe or Ar) and the quenching gas (CO₂ or CH₄). They also depend on the density of the quenching gas and the total pressure.

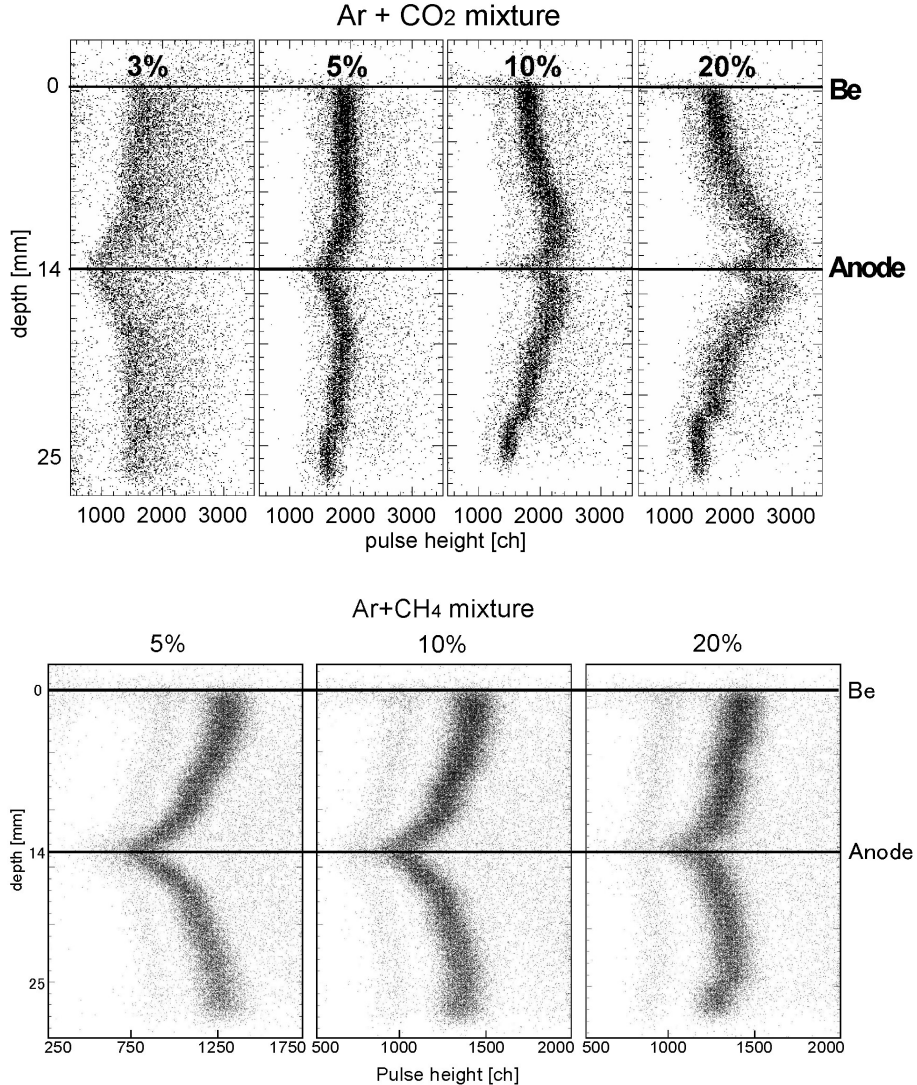


Figure 6. upper: The M-curves of Ar + CO₂ = 3, 5, 10, 20% gases. The curve changes from V-curve to M-curve with increasing CO₂. lower: The M-curves of Ar + CH₄ = 5, 10, 20% gases. The high voltage is 1380, 1488, 1640V, which are chosen to have the similar gas gain. The Ar + CH₄ always shows V-curve, but the depth changes. The X-ray is Cu-K. The counter is HETE gas-flow type (1 atm). The cell size is almost the same as MAXI counter.

3.5. Xe + CO₂ combination

First we reduced the CO₂ as much as possible. The results of CO₂ = 0.2% is shown in Fig. 7 left. It showed V-curve. However, this gas has another big problem of cross talks (§3.6) and cannot be used. We increased CO₂ density as 0.5, 1.0%, and took the M-curves with a similar gas gain. CO₂ = 0.5% gas is almost free from the cross talks. But finally, we took CO₂ = 1% as the gas for the flight counter. It is the safety side of the cross talks problem. It has M-curve, but shows better spectrum than the CO₂ = 3% (Fig. 7 lower).

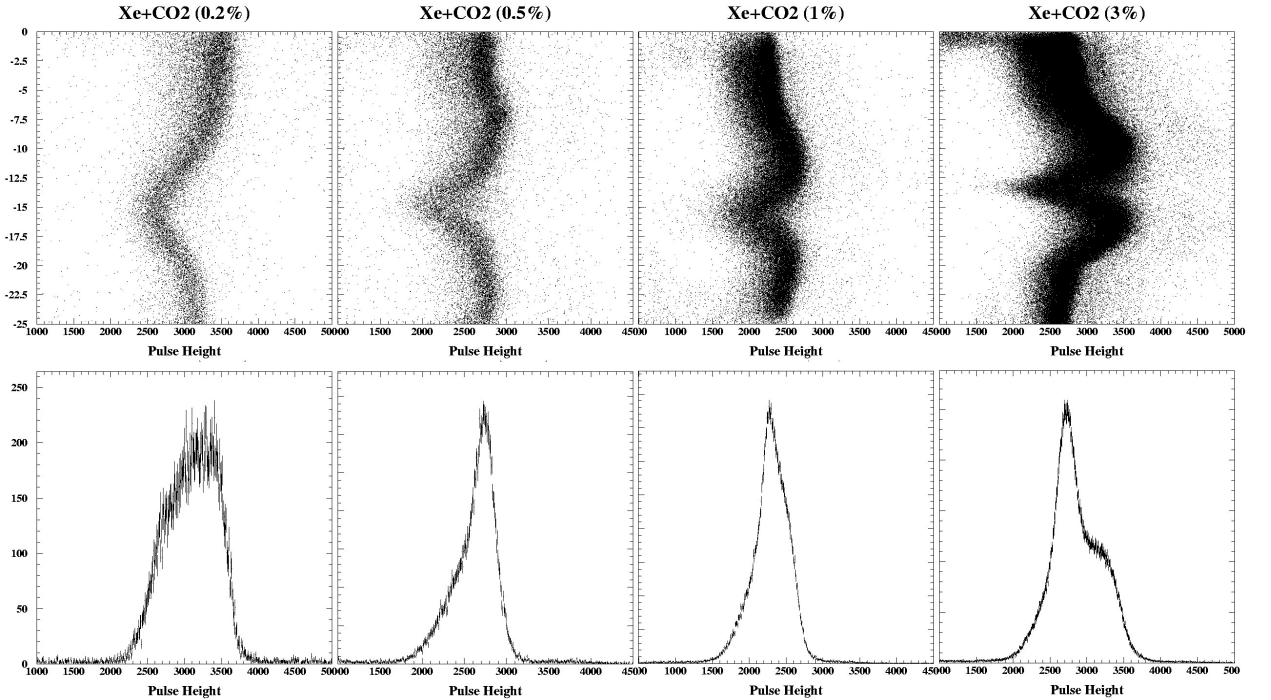


Figure 7. The M-curves of Xe + CO₂ = 0.2, 0.5, 1.0, and 3.0% gases. The gas gains are adjusted to be similar. The X-ray is Mo-K. The lower is the spectra obtained by the projection of the upper curves to the PH axis. The ‘soft tail’ is obvious in CO₂ = 0.2%, and the hard tail is in CO₂ = 3%, which originate from V-curve and M-curve.

3.6. UV lights and quenching gas hypothesis

As cited in §3.3, the additional pulse height of the hard tail is proportional to the square of the gas gain. It suggests a secondary mechanism which is caused by the gas amplification. For example, UV light is one of such candidates. (1) If the amount of the UV lights would be proportional to the gas gain, and (2) if extra electrons are ejected by the UV lights from the quenching gas, the number the extra electrons is proportional to the gas gain. Those electrons are also gas-amplified at the anode, which end up as the additional charges proportional to the square of the gas gain. In this case, ejection of the extra electrons must occur in the vicinity of the anode, because the rise-time of the pulse was faster than 0.5 μ s, and the ejection of the photo electron from the Be window was rejected.

With Xe + CO₂ = 0.2% gas, We had another big problem of cross talks. When Mo-K X-ray was irradiated in one cell, the cross talk appeared in the next cell. The cross talk pulses come in several micro seconds later than the main pulse. The after pulses in the same cell were also seen. The cross talk is considered to be an after pulse to the next cell, which is caused by the photo electrons ejected from the Be window by the UV lights. The several micro seconds is the drifting time from the Be window to the anode. The pulse height of the cross talk is not constant, but 1% of events showed more than 3.7keV pulse heights for Mo-K (17.5keV). The pulse height of the cross talks was roughly proportional to the square of the gas gain. If we consider that the UV lights can reach the Be window, it is the same story as the hard tail. At least, the above hypothesis (1) was proved.

Further study with the Y-scan of the slant beam method revealed follows. The pulse height of the cross talk depends on the X-ray absorbed position in the main cell. When the X-ray stops in the closer side to the Be of the

next cell, it has large cross talk. When it stops in the further side to it, the pulse height of the cross talk is very small. This would be explained by the shadow of the UV lights by the anode. Then the UV lights would be created in a very small region comparable to the anode diameter ($10\mu\text{m}$), and the avalanche would occur in one side, not at all around the wire.

The g_{max} can be understood as the typical position where the most of the UV lights are absorbed by the quenching gas. It is a natural supposition from the fact that we had cross talks and after pulses in the V-curve gas, and not in the M-curve gas. The V-curve happens in the insufficient quenching when the UV lights can reach the Be window. There is not a proof for the hypothesis (2), but some of the quenching gas would eject electrons, or excited quenching gas would have smaller work function to produce electrons and eject electrons with smaller collision energy. This could be an explanation candidate for the anomalous gas gain.

3.7. Shape of electron cloud hypothesis

An interesting relation was found between M/V-curves and the shapes of electric clouds. Fig. 8 upper is the simulated distribution of the electrons when the first electron reaches the anode (by the garfield software). In the $\text{Ar}+\text{CO}_2 = 3\%$ gas, the near-anode event has round shape, but the window event has an elongated shape along the wire (wide), which has considered to have less space-charge effect. Then it had V-curve. In the $\text{Ar}+\text{CO}_2 = 20\%$ gas, the near-anode event has round shape as well, but the window event has an elongated shape vertical to the wire (high), which is considered to have more space-charge effect. Then the curve is M-curve. By the mechanism of the space-charge effect the gain curve may be related to the width/height ratio. Fig. 8 lower are the graphs for $\text{Ar}+\text{CH}_4$, $\text{Ar}+\text{CO}_2$, and $\text{Xe}+\text{CO}_2$. Compared with Fig. 6 and Fig. 7, the curves are very similar. However, the relation between the space-charge effect and the width/height ratio is not clear.

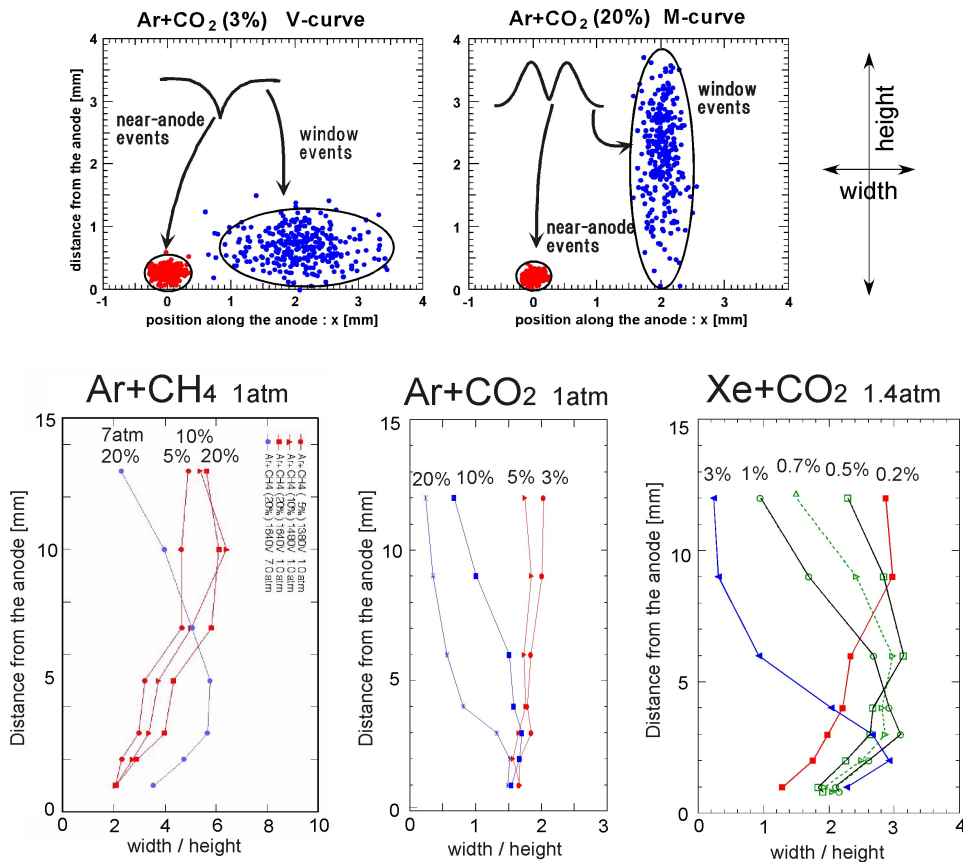


Figure 8. upper: The simulated image of the electron cloud when the first electron reaches the anode in $\text{Ar}+\text{CO}_2 = 3\%$ and 20% gases. 1000 electrons were tried. lower: The simulated width/height ratios for various gas mixtures. Y-axis is the position where the X-ray is absorbed.

4. PERFORMANCE OF THE ENGINEERING (EM1) COUNTER

As discussed in the previous sections, we decided to use $\text{CO}_2 = 1.0\%$ for the flight counter. The engineering counter (EM1) was built by Metorex Company, Finland, and delivered to RIKEN in April 2001. It is called ‘engineering’, but actually the first counter of the flight model. It has the flight quality and have a little possibility to be launched. The results are shown in the figures; the Energy linearity (Fig. 9 left), the HV-PH relation (Fig. 9 right), the Energy resolution (Fig. 10 left), the Position resolution (Fig. 10 right), the Position error (Fig. 11), and the Gain uniformity (Fig. 12). P3 and P4 are points on the counter; P3 ($X=-5\text{mm}$, $Y=0\text{mm}$ on-wire), P4 ($X=-5\text{mm}$, $Y=14\text{mm}$ off-wire).

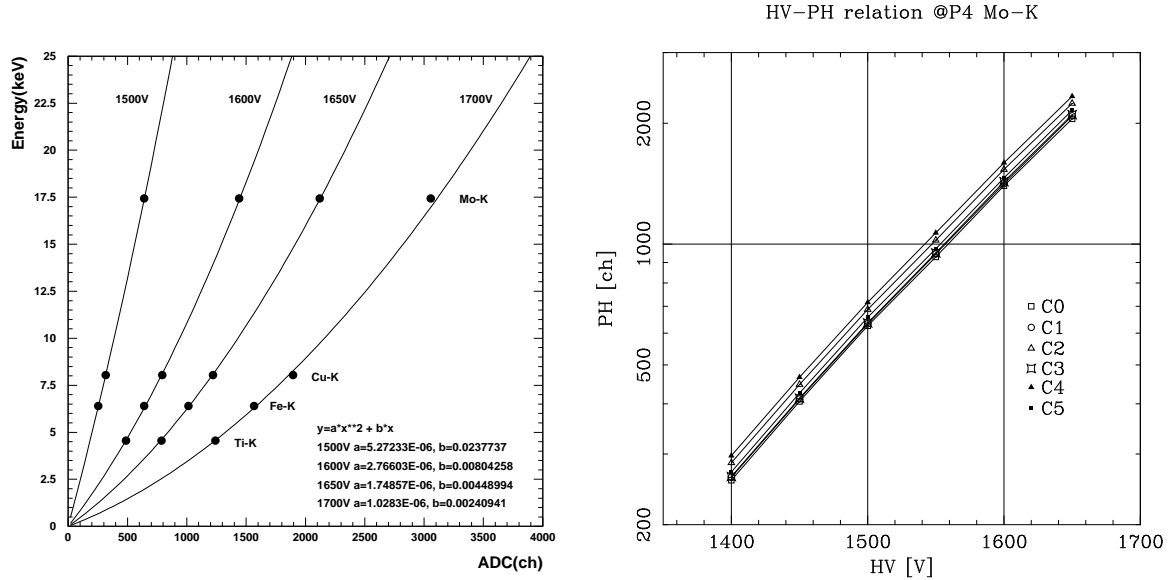


Figure 9. left: Energy linearity was measured at P3 (Ti-K, Fe-K, Cu-K) and P4 (Mo-K) in 1500, 1600, 1650, 1700V. The measurement at P4 is used for Mo-K to get rid of the hard tail effect. For the others the effect is small, since their X-ray stops very closely to the Be window. The curve is the fit with the $E = aPH^2 + bPH$. right: The HV-PH relation at P4 with Mo-K. The six anodes have similar gain. The curves start to bend at 1550V.

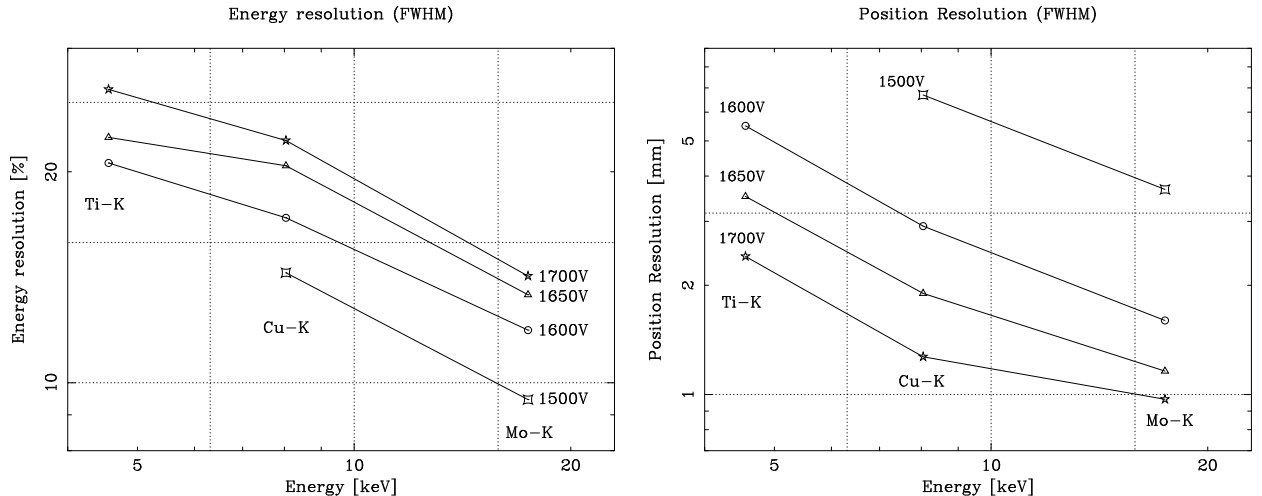


Figure 10. left: Energy resolution at P3 (Ti-K, Fe-K, Cu-K) and P4 (Mo-K). The energy linearity in Fig 9 left is considered. The data points roughly on the line of $\propto E^{-0.5}$, which is the case dominated by the statistics of the primary electrons. In higher voltage, gain difference in the cell or other reasons degrade the energy resolution. right: Position resolution. The data of Ti-K and Cu-K has the relation of $\propto E^{-1}$. This is when the position resolution is dominated by the noise (mainly Johnson noise). Actually it is $\propto PH^{-1}$. The position resolution saturated at 1.0mm.

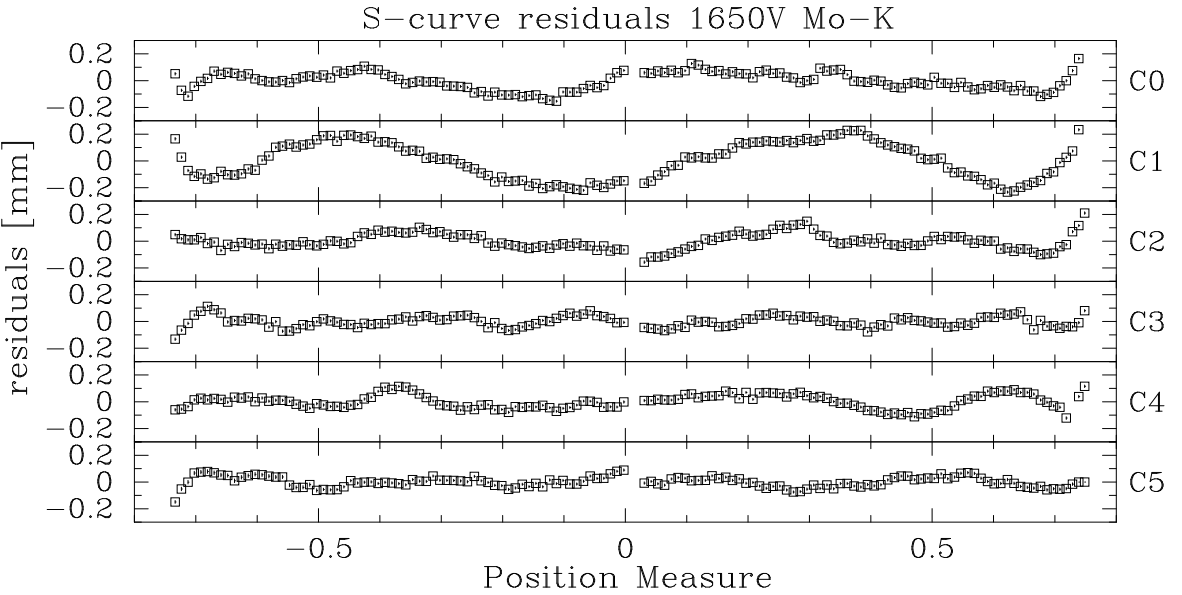


Figure 11. The position measure of each anode is fit by $X = a_0 + a_1 PM - a_2/(PM - a_4) - a_3/(PM - a_5)$. These are residuals from the bestfits. The data points are $X = -135 \sim 135$ mm by 2 mm step. This empirical equation represents the curve within ± 0.2 mm. Since these residuals are proper to the anode, we will correct these to obtain more precise position.

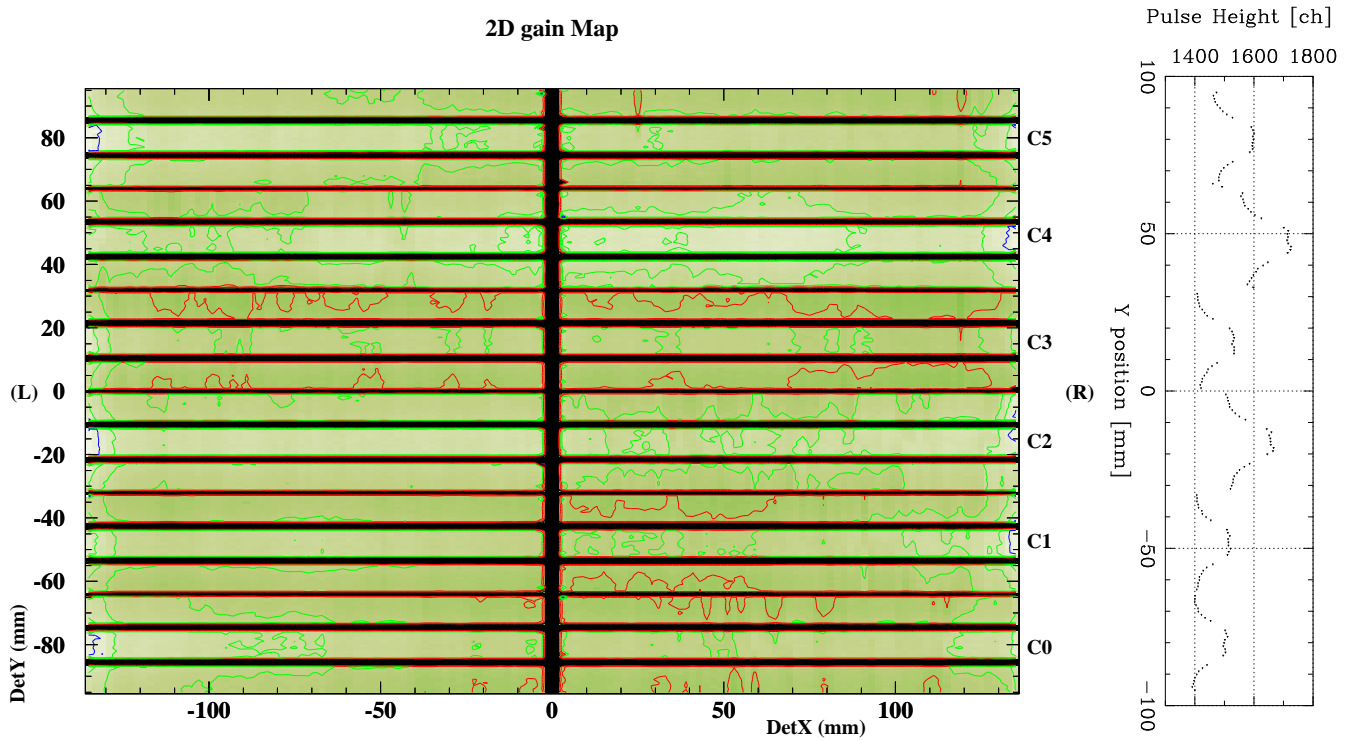


Figure 12. This is the gain map of EM1 counter obtained by Mo-K at 1600V. X-ray was irradiated in every 2×1 mm grids. The color level is 10 steps in 1000–2000 ch. The gain was uniform within $\pm 5\%$ in one cell. The gain difference of the anodes was $\pm 7\%$. We selected the carbon wires of similar resistances and mounted them in one counter to achieve a uniform gain. The right is the cross section at $X = -5$ mm (P3). The high gain near the anode is due to the hard tail.

5. OBSERVATION SIMULATION

Based on the obtained performance of the test and EM1 counters, we performed the simulations of MAXI/GSC observations [8]. First, we consider instrumental properties for the whole assembled system (§5.1). The second part deals with scanning of any sources with given celestial coordinates in the sky by considering the ISS orbital motion and integrating all the GSC units (§5.2). Simulations of X-ray backgrounds by the cosmic X-ray background and the cosmic charged particles are described in §5.3.

5.1. Simulations of source scanning with GSC

Let's consider a source moving into the FOV of a slit collimator as the camera moving across the sky. Exposure T is defined as the time duration between the source moving into and moving out off the FOV (~ 3 deg) in the θ direction (for the simple case for the central GSC units, $T \sim 3$ deg/ $\omega \sim 45$ s where ω is the angular velocity of the ISS of 4 arcmin s $^{-1}$). The Monte Carlo simulation was designed for the scanning processes of a source with constant X-ray flux density f_x , at elevation angle ϕ , and with exposure T .

Firstly, a series of incident photons onto the GSC slits is simulated within time T , in a way that the time interval δt of two successive photon events following exponential distribution, as expected from the Poissonian statistics of photon emission/absorption processes. Each photon is registered with the arrival time t_i , energy E_i , and incident position on the slits. E_i is drawn from the ultimate spectral energy distribution of the X-rays before detection. The azimuth angles of the incident photons can then be determined from their arrival time t_i . With the photon incident aspect and energy known, we can trace each photon along its path into the collimator, and subsequently, the detector window and gas counter. A photon is discarded if it either fails to pass through the collimator, or is absorbed in the Be-window, or penetrates the anode cell. Survival photons are taken as ‘detected’ X-ray events.

Laboratory calibration data for the energy–pulse height relation and the energy resolution (pulse height fluctuations) were used for converting the photon energy to pulse height in the gas counters. The position dependence of the gas gain or ‘hard-tail effect’ (§3, [6]) was taken into account properly. The ‘measured’ absorption positions of photons are converted from the ‘actual’ position X in ray-tracing by using the calibrated position measure vs. X relationship.

5.2. Putting all together

Next we calculated the trajectories of stars moving across the FOV of slit camera in the scanning processes for both the forward and the zenithal views, using the information of the ISS orbits and the attitude of the GSC units. This enables us to determine, for a star at any given celestial position in the sky, the time of starting to move into the FOV, the exposure T , and the elevation angle ϕ , i.e. the parameters needed as inputs for the simulations of source scanning/detection. As a useful example, we show in Fig. 13 the exposure time of sources as seen by the three GSC units in one FOV. For the two side GSC units, the exposure time depends on the latitude of a star in the orbital coordinate systems, but it is constant for the central unit.

By combining these results with the above scanning/detecting processes, we are able to simulate complete scanning processes of the whole sky with the MAXI/GSC, by assuming a population of celestial X-ray sources. The simulated ‘observational’ data comprise photon registration time, left and right pulse heights (thus the position measure), the detector and anode IDs. The spatial and energy information of the X-ray sources can be re-constructed by analysis of these data.

5.3. Backgrounds

There are two methods for the simulations of the cosmic X-ray background (CXB). One is to divide the whole sky into grids with elements which are much smaller than the point spread function of the GSC, and then to treat each element as a point source; however, this is CPU-time consuming. Alternatively, we used another method by taking the advantage of the CXB isotropicity. The idea is that, during the scanning processes, the detectors are seeing the diffuse background emission with the same X-ray brightness*, regardless of which part of the sky is actually being seen. The expected photon flux density at the slits within a solid angle in any direction in the FOV can be obtained and the above simulations of photon detection are used.

*In fact this is not the case as the CXB is modified by Galactic absorption in the soft X-ray band. However, this effect is not significant in the whole MAXI/GSC energy band for most part of the sky, and, if needed, can be compensated ultimately by using Monte Carlo drawing if the probability of absorption, or optical depth, is known.

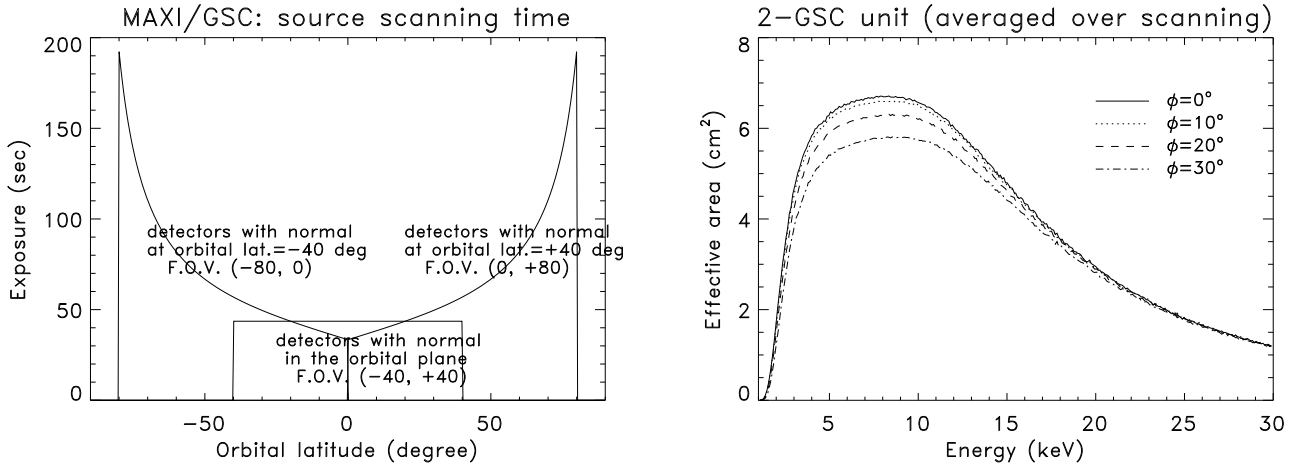


Figure 13. left: Source exposure time as functions of source orbital latitude for three GSC units in one (forward or zenith) view. A source can be seen by one or two units depending on the orbital latitude and is scanned twice by two FOVs successively in one complete orbit. The exposure time is the full width at bottom of the scan profile. right: Effective area of 1 center unit (2 cameras), averaged while a source moves across FOV by the scanning. ϕ is the photon incident angle relative to the detector normal. The low energy transmission is limited by the Be-window. The difference of the effective areas in 2–15 keV is by the decrease of the slit area with ϕ . The difference becomes smaller at higher energies by the compensation effect, i.e. the stopping power increases at larger ϕ because the travel length in the gas is longer.

The simulation of detector background (DBG) caused by cosmic charged particles is straightforward, but is uncertain due to the unknown intensities of these particles in orbit. We assumed in our simulations a power law spectrum for the DBG with a photon index $\Gamma=0$ in 1–30 keV and normalization as two times as the room background, which is $2 \times (4.5 \times 10^{-4}) \text{ c s}^{-1} \text{ cm}^{-2} \text{ keV}^{-1}$ at 1 keV. This is the value after the anti-coincidence between carbon anodes, and carbon anode and veto.

6. RESULTS OF SIMULATIONS

The first-hand outcomes are simulated photon events data resembling the read-out given by the on-board processors, namely, the time and the IDs of detectors/wires of photon, the pulse height channels of left and right readouts, which can be used as inputs for the MAXI data analysis tools. Moreover, the simulation code can also be used to examine and quantify some instrumental characteristics, and to produce anticipated ‘scientific results’ by analysis of the simulated data.

6.1. Effective area and point spread function

The detection efficiency, or effective area A_{eff} for the assembled system can be obtained by a direct comparison of the detected and source counts. It is dependent on photon energy E and photon incidence aspect, i.e. $A_{\text{eff}}(E, \theta, \phi)$. Since MAXI operates in a scanning mode in which a source moves across the FOV with θ varies from $-\theta_{\max}$ to θ_{\max} , it is more meaningful to use the effective area averaged over θ , i.e. $\langle A_{\text{eff}} \rangle(E, \phi)$. We show in Fig. 13 the averaged $\langle A_{\text{eff}} \rangle(E, \phi)$ for a unit as a function of photon energy at several ϕ angles. The virtue effective area with respect to a given source depends on the number of GSC units (either 1 or 2, see Fig. 13) which are actually seeing the source as well as the respective ϕ angles, both determined by the source position and the ISS orbit.

The point spread function (PSF) can be derived by mapping the spatial distribution of detected events from an input point source on the detector X (anode) and Y (scanning direction, or time) space, and much meaningfully, de-projected back onto the $\theta - \phi$ space. Fig. 14 shows the PSF at 8 keV photon energy for sources with incident angle $\phi = 0^\circ$ (left) and 20° (right), respectively. At large incident ϕ angles, a tail emerges (right panel) with the extent increasing with ϕ , which results from slant incidence of photons and becomes prominent for photons with higher energies, i.e. larger mean free paths in the gas counter.

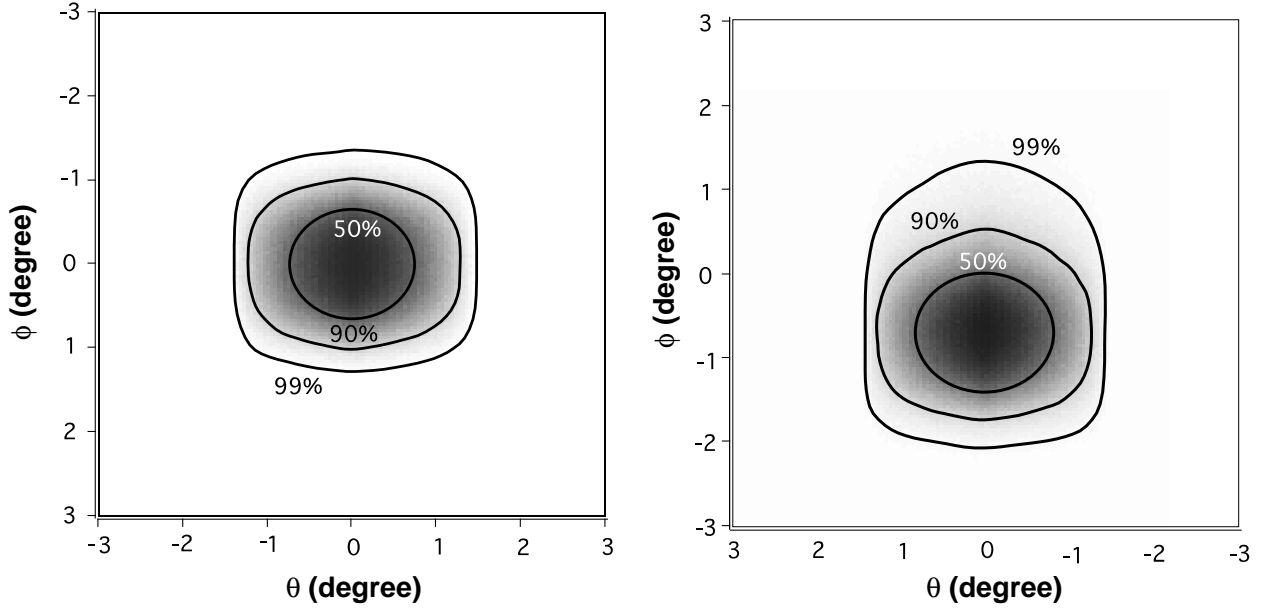


Figure 14. Profile of the GSC response function for a point source on the orbital longitude (vertical) – latitude (ϕ , horizontal) plane for 8 keV photons, derived from the simulations. Left panel: $\phi = 0$ deg. Right panel: $\phi = 20$ deg. at large ϕ a tail appears in the ϕ direction for high energy photons caused by slant incidence of photons.

6.2. Crab count rate and in-orbit data rate

One good indicator of the capability of X-ray detectors is the yielded count rate in observing the Crab Nebula—the standard calibration source in X-ray astronomy. As a useful example, we listed in Table 1 the simulated Crab count rate as observed with one GSC in the 1–30 keV band for various off-axis angle ϕ . For on-axis scanning ($\phi = 0$ deg) this yields $\sim 10 \text{ c s}^{-1}$ per GSC in 1–30 keV when averaged over the scan time. Note that 4 GSC observe the source, if the orbital latitude is within ± 40 degrees. Then the average count rate is $\sim 40 \text{ c s}^{-1}$. Incorporating the source exposure in Fig. 13 one may have a rough estimate about source counts accumulated in the scanning with the MAXI/GSC. Then by scaling the source fluxes to that of Crab (1 Crab = $4 \times 10^{-8} \text{ erg s}^{-1} \text{ cm}^{-2}$ in 1–30 keV), we can know the flux of the source.

Table 1. Simulated GSC count rate for the Crab Nebula (1–30 keV)

| ϕ angle (deg) | count rate (c s^{-1}) |
|--------------------|----------------------------------|
| 0 | 9.9 |
| 10 | 9.6 |
| 20 | 9.1 |
| 30 | 8.1 |

When the Crab passes in a GSC camera. Averaged over the scan time. The peak count rate in the triangular scan profile is double of the value above.

Table 2. Simulated in-orbit GSC data rate (one orbit, 1–30 keV)

| | counts ^a (10^4 c) | CR ^b (c s^{-1}) | units ^c |
|----------------------|---------------------------------------------|------------------------------------------|-------------------------|
| Crab ^d | 0.33 | 8.1/9.7 | central/left x 2 views |
| Sco X-1 ^e | 3.0 | 71.4/87.1 | central/right x 2 views |
| CXB | 10.3 | 1.6 | all (6 units) |
| DBG | 87.7 | 13.5 | all (6 units) |
| Total ^f | ~ 104 | ~ 16.0 | all (6 units) |

- a. The total counts accumulated in one orbit.
- b. The mean count rate per GSC, averaged over the scan time.
- c. The unit with which the source is in FOV. One unit has 2 GSC.
- d. Assuming an orbital latitude -29 deg.
- e. Assuming an orbital latitude 32 deg and Crab-like spectrum.
- f. CXB+DBG+HEAO-1 sources with Crab-like spectra assumed.

The estimation of data rate is important in designing the on-board signal processing electronics and telemetry, as well as estimation of the dead time for strong X-ray sources. This can be easily obtained from the simulations. We show in Table 2 the estimated data rate for the total 12 GSC for one orbit data-taking. It should be noted that, however, since the ‘detected’ counts are dominated ($\sim 85\%$) by detector particle background, the estimated total counts depend strongly on the assumption on the DBG rate. The values given in the table 2 were obtained based on the above DBG model in §5.3, and should be taken as a reference value only. More accurate estimation has to rely on more realistic modeling/measurement of the DBG.

6.3. Simulations of scientific results of MAXI

For demonstration purpose we show here examples of simulated observational results of the MAXI/GSC. Fig. 15 shows simulated X-ray light curves of the Galactic neutron star binary (burster) X1608-52 (left) and the Seyfert galaxy MCG-06-30-15 (right) for one month data-taking. A power law photon index of -1.9 and -1.8 was assumed in the MAXI band for X1608 and MCG-06-30-15, respectively. The detector backgrounds were subtracted. The input data are from ASCA observations of the two sources, respectively.

Fig. 16 shows the all-sky X-ray image obtained with the MAXI/GSC for five months data-taking, with the detector particle background subtracted. The input X-ray sources are from the HEAO-1 source catalog as well as the CXB.

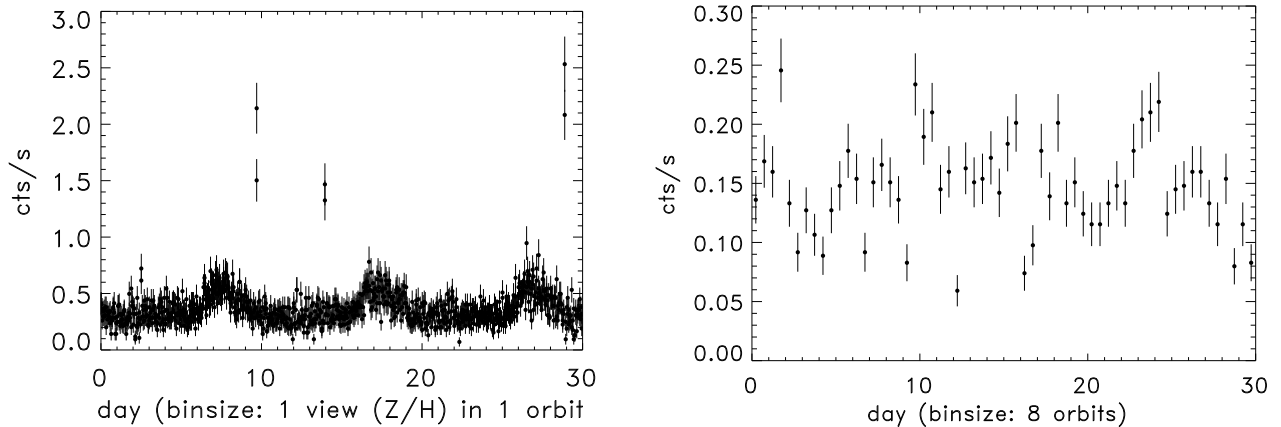


Figure 15. Simulated X-ray light curves for the X-ray burster X1608-52 (left) and the Seyfert galaxy MCG-06-30-15 (right) for one month data-taking. Sources are assumed to be at orbital latitudes of 10 degree and the precession of the ISS orbit is not taken into account. For X1608-52, the time bins represent data samplings in each view (two views in one orbit). X-ray bursts and orbital intensity modulation are seen. For MCG-06-30-15 each time bin represents 8 ISS orbits. Each flare and the long-term variation are seen. Input data are from ASCA observations (X1608: data credit Dotani; MCG-06-30-15: data credit Negoro).

7. SUMMARY

The MAXI mission was introduced and the design of the GSC flight-model counter was shown. The detailed investigation on the hard tail was explained. The M-curves of $\text{Xe}+\text{CO}_2$, $\text{Ar}+\text{CO}_2$, and $\text{Ar}+\text{CH}_4$ were presented with various CO_2/CH_4 densities. The anomalous gas gain might occur when the quenching gas absorbs the UV lights near the electron-avalanche region. Or it might be by the space-charge effect depending on the shape of the electron cloud. The engineering model counter (EM1) was made and tested. The various results were shown, which was almost as expected. We are ready to move on to the production phase of GSC flight model. The observation simulation was performed and the current results were summarized.

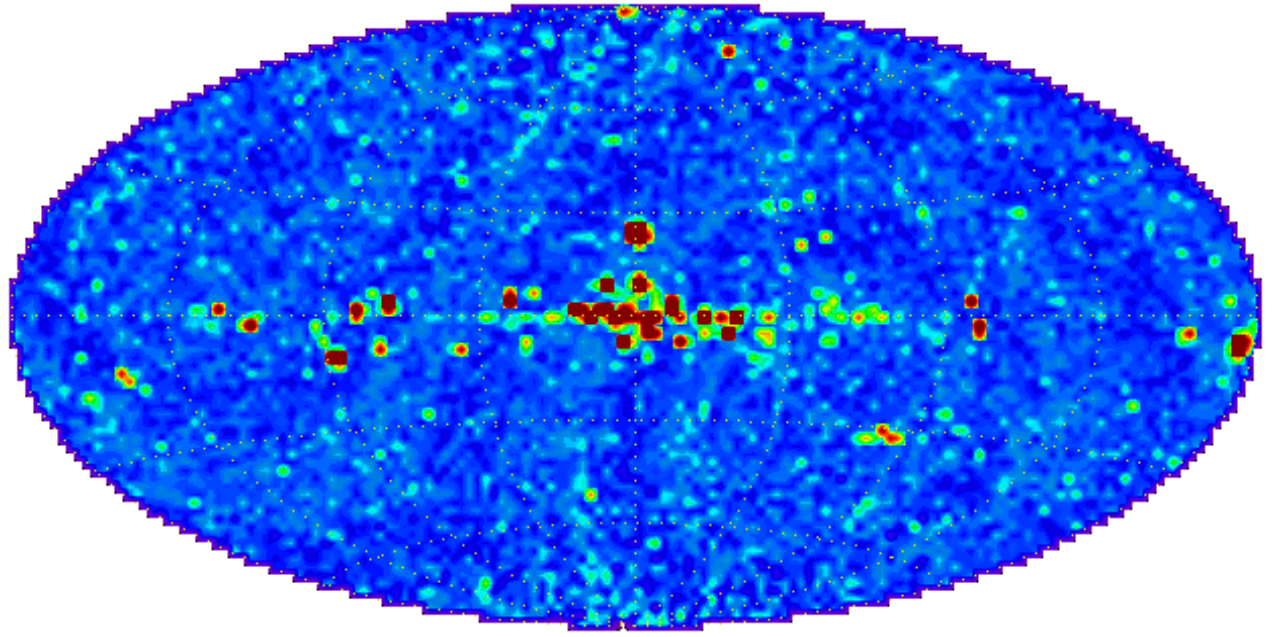


Figure 16. All-sky X-ray image (Galactic coordinate) obtained with the MAXI/GSC for five months data-taking, with the detector particle background subtracted. The inputs are the HEAO-1 X-ray source catalogue and the cosmic X-ray background. The absorption and diffuse emission of the Galactic plane were not included. Instrumental effects such as aspect-dependent exposure and effective area were not corrected.

REFERENCES

1. M.Matsuoka, et al. “MAXI for JEM on the Space Station,” *Proc. SPIE* **3114**, pp. 414, 1997.
2. K.Torii et al. “X-ray detectors and calibration system for the MAXI mission,” *Proc. SPIE* **3765**, pp. 636, 1999.
3. T.Mihara, M.Matsuoka, N.Kawai, A.Yoshida, H.Tsunemi, E.Miyata, H.Negoro, K.Torii, S.Ueno, M.Sugizaki, H.Tomida, I.Sakurai, Y.Shirasaki, M.Yamauchi, “Monitor of All-sky X-ray Image (MAXI),” *Proc. Space Technology and Applications, International Forum 2000*, pp. 181-186, 2000.
4. H.Tomida, M.Matsuoka, S.Ueno, K.Torii, M.Sugizaki, W.M.Yuan, S.Komatsu, Y.Shirasaki, N.Kawai, A.Yoshida, T.Mihara, I.Sakurai, H.Negoro, H.Tsunemi, E.Miyata, M.Yamauchi, I.Tanaka “ The MAXI Mission on the International Space Station,” *Proc. SPIE* **4012**, pp. 178-185, 2000.
5. I.Sakurai, T.Mihara, N.Kawai, A.Yoshida, Y.Shirasaki, M.Matsuoka, M.Sugizaki, and T.Kamae “Dependence of Gas Gain on X-ray-absorbed Position in Proportional Counter,” *Proc. SPIE* **4140**, pp. 511-519, 2000.
6. Y.Shirasaki, et al. “Performance of the wide-field x-ray monitor on board the High-Energy Transient Explorer 2,” *Proc. SPIE* **4012**, pp. 166-177, 2000.
7. S.Ito, et al. “Gas amplification of proportional and SQS modes observed as a function of the radial distance of the position of primary ionization,” *NIM* **A348**, 297, 1994.
8. W.Yuan, M.Matsuoka, et al. “Simulation of Observations and Data of MAXI,” *Proc. MAXI Symposium on AGN Variability*, Nikko, 2001.